Growth Kinetics of Calcareous Deposits on Thermally Sprayed Aluminum Coatings in Natural Seawater

Edgar Hornus,[‡,] Francisco Vouilloz,[*] Yu Long,[*] Kjetil Andersen,[**] Ola Krosness,[**] Mike King,[***] Roy Johnsen,[****] Mobin Salasi,[*] and Mariano Iannuzzi[*]*

The formation of calcareous deposits on thermally sprayed aluminum (TSA)-coated surfaces immersed in natural seawater and connected to a cathodic protection system is a recurring issue. There is at present limited knowledge on the calcareous deposits' formation kinetics on TSA in natural seawater following prolonged exposure at different temperatures. In this study, bare 25Cr super-duplex stainless steel (SDSS) and TSA-coated SDSS tube coupons (with and without a silicone-based sealer) were exposed to natural seawater under potentiostatic cathodic protection (CP) and open-circuit potential (OCP) conditions at different temperatures (i.e., 20°C, 35°C, 60°C, and 80°C) for 1.5 y. The coupons were extracted at various intervals to construct growth kinetics curves under various test conditions. The deposits were subsequently examined using scanning electron microscopy, energy dispersive spectroscopy, and x-ray diffraction. For all of the specimens, the deposits' areal coverage and thickness on the exposed surfaces increased with exposure time. Fewer deposits were seen under CP conditions than OCP at low temperatures (20°C and 35°C), whereas more deposits were observed with CP than those at OCP at high temperatures (60°C and 80°C). Last, a recommended protection potential of −0.90 V_{SSC} ($V_{Ag/AgCl}$) and cathodic current density values of −8 mA/m^2 and −15 mA/m^2 were obtained based on the findings of this study.

KEYWORDS: calcareous deposits, cathodic protection, thermal spray coatings

INTRODUCTION

In the oil and gas industry, thermally sprayed aluminum (TSA) coatings are commonly used, primarily, to reduce anode demand in cathodic protection systems (CP) and impart some degree of sacrificial protection in the topsides and splash zone areas.[1-2] The use of TSA coatings has advantages in systems where long service life is required. TSA coatings are also used to reduce the formation of calcareous deposits, normally a combination of $CaCO_3$ and $Mg(OH)_2$, on heat exchanger piping.[3-4] While the formation of calcareous deposits reduces the current demand for the CP system,[3,5-6] there are some major drawbacks. For example, the formation of calcareous deposits on subsea heat exchangers must be prevented or minimized due to the deposits' low thermal conductivity, which would reduce heat transfer efficiency.

The goal of this investigation was to quantify the calcareous deposit precipitation rate and characteristics (i.e., deposit thickness, composition, and morphology) on different TSA-coated and bare 25Cr super-duplex stainless steel (SDSS) (UNS S32750[(1)]) surfaces as a function of temperature in natural Western Australian seawater. Long-term tests were performed on different substrates, namely, bare 25Cr, SDSS coated with TSA (99.5% Al), and SDSS coated with a sealed TSA layer at the open-circuit potential (OCP) and with a potentiostatic cathodic protection system. The thickness and morphology of the calcareous deposits were investigated at different substrate temperatures. In addition, optimal protection current density and corrosion potential are recommended based on the results.

EXPERIMENTAL PROCEDURES

Tubular SDSS specimens—19.05 mm(¾ in) diameter—with the following specimen conditions were tested:

(i) Bare 25Cr coupons (B),
(ii) TSA-coated coupons (TSA, without sealer),
(iii) TSA-coated coupons with sealer (TSA/S)

The SDSS 25Cr tubes were externally coated (the surface exposed to the seawater) with commercial TSA and TSA with a sealer by a certified coating applicator, as per the Original Equipment Manufacturer's specifications. Intertherm®[†] 179 was used as the sealer, which is a heat-resistant silicone-based resin. Upon delivery, each tube was cut in two sets of (a) 3 units, 10 mm long and (b) 14 units, 50 mm long. The short coupons were used for as-received coating characterization, and the longer coupons were used for the immersion tests.

Submitted for publication: May 2, 2022. Revised and accepted: November 3, 2022. Preprint available online: November 3, 2022, https://doi.org/10.5006/4118.
[‡] Corresponding author. E-mail: edgar.hornus@curtin.edu.au.
[*] Curtin Corrosion Centre, Perth, Western Australia 6102, Australia.
[**] Aker Solutions, Norway.
[***] Wood Plc Perth, Western Australia, Australia.
[****] Norwegian University of Science and Technology, Trondheim, Norway.
[(1)] UNS numbers are listed in *Metals & Alloys in the Unified Numbering System*, published by the Society of Automotive Engineers (SAE International) and cosponsored by ASTM International.
[†] Trade name.

AQ1

ISSN 0010-9312 (print), 1938-159X (online)

The tests were performed in filtered (filter pore size of 500 µm) natural seawater at four different temperatures: 20°C, 35°C, 60°C, and 80°C. In this regard, seawater was filtered before entering the tanks to remove suspended solid particles exclusively. The coupons were immersed in four separate 200 L tanks (i.e., one per temperature). The tanks were placed in Curtin Corrosion Centre's SeaLab and exposed only to artificial light. The external tank's surfaces were painted to maintain maximum darkness inside the tanks, preventing the proliferation of photosynthetic microorganisms. The water in the tanks was continuously replenished at a flow rate of 1.2 L/h, so all of the seawater was replaced every 7 d. Table 1 presents the composition of the natural seawater used for the testing. For the seawater analysis, water samples were collected from an external seawater tank (70,000 L capacity) that supplies the SeaLab at Curtin University. The main tank was replenished from surface seawater (from approximately 1 m depth) from Hillarys Boat Harbour, Western Australia.

A stirrer system was added to each tank—located in the center of the containers—to maintain a uniform temperature distribution and to provide some degree of water circulation. The rotational velocity of the impellers was set at 60 rpm. Studying the effects of flow velocity was not in the scope of this research. Titanium Gr. 2 shaft stirrers were fixed to the lid with two PTFE (Polytetrafluoroethylene) supports. The titanium shafts (1,000 mm in length) had a semicircular end to act as a single impeller. The entire shaft was made from the same material in one piece.

Six holders per tank with a capacity of six coupons each were used, as shown in Figure 1. The coupons were positioned vertically inside the tank and held from the 3-in caps over the lid. The holders were made using a tubular-shaped PTFE section with an outer-diameter (OD) similar to that of the test coupons. Only the outer face of the tubular specimens were in contact with the electrolyte. To supply the cathodic current, two graphite anodes 1-in diameter and 750 mm long each were located near the tank walls. One silver/silver-chloride/(SSC) seawater reference electrode was located next to each sample holder (up to six reference electrodes per tank). Figure 1 depicts a 3D–CAD rendering of a tank setup (without the heating and cooling elements for better visualization) and the fully assembled holder distribution. Figure 1 also shows NEOPRENE®† square washers placed between the samples and the PTFE parts.

The current of the coupons polarized at −1.050 V_{SSC} was measured during exposure. A rectifier was used to apply the cathodic potential. A voltage divider electrical circuit was used to measure the cathodic current. The circuit allowed for switching the resistor from 1 Ω to 100 Ω to improve the accuracy of the measurements. A 10 Ω resistor was used to measure the current of the polarized coupons. The wire connections were soldered at the inner surface of the samples and placed inside and along the sample holder, unexposed to the environment (Figure 2).

For the freely exposed coupons, the OCP was recorded against Ag/AgCl/seawater reference electrodes. After the acquisition, the potentials were converted to a conventional Ag/AgCl/KCl saturated reference electrode. Ten data acquisition modules Zen RTU Mini®† with 16 universal isolated inputs were used giving 160 independent channels to measure a difference potential or current. All data were recorded each hour.

The gravimetric study was performed using an analytical balance. The coupons' weight was determined before and after exposure to construct the calcareous precipitation rate curve and was measured together with the wire connectors before and after retrievals. Prior to the measurements, the coupons were dried in a convection oven at 40°C for 24 h. This process was repeated until no change in weight was observed. At that point, coupons were considered thoroughly dried, and the values were recorded. Light optical microscopy (LOM) and scanning electron microscopy (SEM) coupled with energy-dispersive spectroscopy (EDS) were used to characterize the morphology and composition of the calcareous deposits. Subsequently, crystallographic XRD measurements were performed with a Bruker D8–Advanced (Bruker, Billerica, MA) using Cu-Kα radiation and collecting data over the 2θ range of 0° to 80°.

Table 1. *Seawater Composition Measurements from ARL Laboratory*

Reference	Unit	Concentration
Barium: Dissolved	mg/L	0.02
Calcium: Dissolved	mg/L	570
Iron: Dissolved	mg/L	<0.01
Magnesium: Dissolved	mg/L	1,800
Potassium: Dissolved	mg/L	820
Sodium: Dissolved	mg/L	9,300
Strontium: Dissolved	mg/L	8.6
Chloride	mg/L	20,000
Fluoride	mg/L	1.1
Sulfate	mg/L	2,700
Bromide	mg/L	79
Alkalinity	mg $CaCO_3$/L	130
Bicarbonate	mg $CaCO_3$/L	130
Carbonate	mg $CaCO_3$/L	<5
pH	pH units	8
Total Dissolved Solids	mg/L	36,000

After exposure, about 60% of each coupon was mounted in an epoxy resin to protect the deposits on the tubular specimens' outer surface. After the low-temperature exposures, a biofilm appeared on the surface, looking like rust deposits (Figure 2). The specimens were cross sectioned with a precision cutting machine. Three 10-mm thick slices were obtained from each tubular specimen, Figure 3(a). Each slice was wet ground from 80 to 600-grit SiC paper. The specimens were rinsed with ultrapure water, degreased with ethanol, and dried with high-purity nitrogen gas.

The thicknesses of the deposits over the TSA coatings and that of the TSA layer were measured with a LOM. Darkfield images were taken to increase the contrast between the deposit and the mounting resin. Images were taken at different angular orientations to account for the seawater flow. Figure 3(b) illustrates a schematic of the top view of deposits. In each cross section, a total of 12 independent measurements and 12 TSA thickness measurements were obtained per coated specimen.

Two approaches were used to determine the thicknesses of the calcareous deposits as a function of immersion time, i.e., (a) measuring cross sections and (b) estimation from

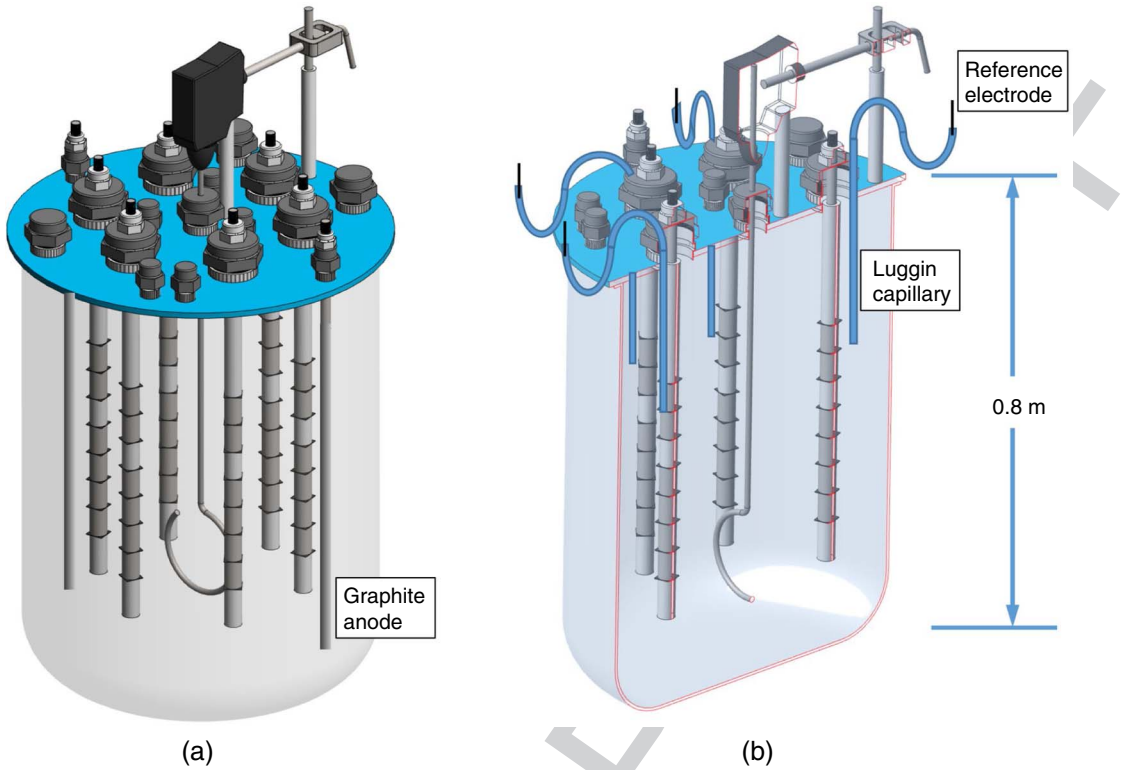

FIGURE 1. *(a) The tank design setup showed as a 3D CAD scheme with the fully assembled sample holder distribution (six per tank), the graphite anodes position (two per tank), and (b) tank cut view with Luggin capillary and reference electrode position (one per holder). Heating and cooling elements were not drawn.*

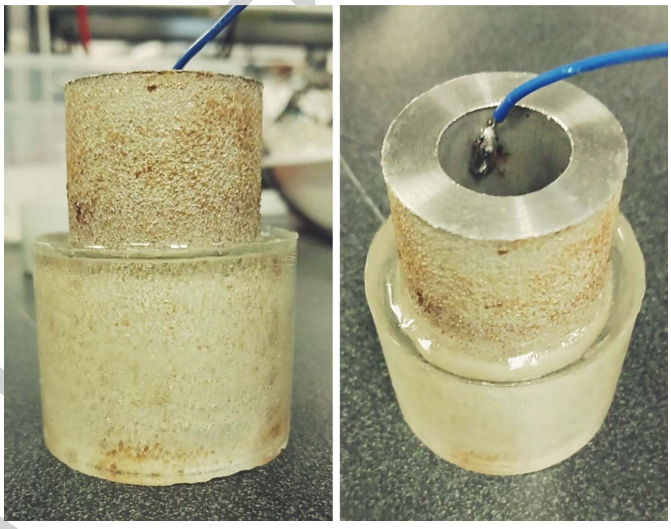

FIGURE 2. *Pipe specimen after the retrieval, embedded in epoxy resin. A thin layer of biofilm formed on the surface of the specimen, which was not visible at higher temperatures. There is no rust on the surface; the samples were cathodically protected.*

weight gain (assuming a constant thickness) using the calculation method given in Figure 4. For this study, we used both methods, but considering the nonhomogeneity of the deposits, the deposit thickness values were derived from the overall weight gain and are reported in this paper. Pure aragonite ($CaCO_3$) and brucite ($Mg(OH)_2$) densities were considered for thickness estimation from the weight gain, and Al dissolution/corrosion products were not considered in the calculations.

RESULTS

3.1 | Thermally Sprayed Aluminum Coating Characterization

Figure 5 shows a LOM micrograph of a TSA coupon. In the figure, pores and surface undulations associated with the TSA deposition process can be seen. These features were observed in the remaining coupons as well. In this regard, the Direct Comparison procedure (test method A) of the ASTM E2109-01

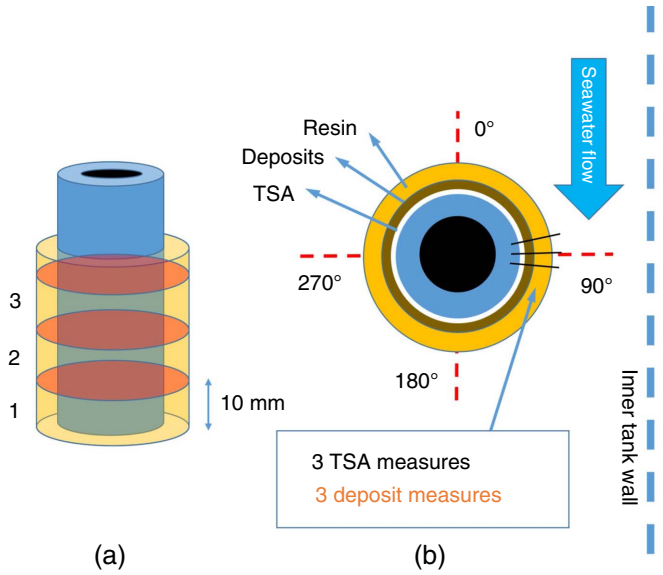

FIGURE 3. *(a) Cutting slices scheme and (b) measurement scheme (one measurement was taken at 0°, 90°, 180°, and 270°) for three transverse slices through the specimen.*

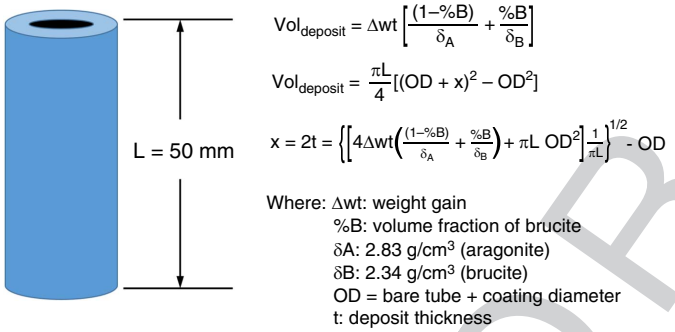

FIGURE 4. *Calculation of deposit thickness from the weight-gain measurements. Pure aragonite and brucite densities were only considered, and Al dissolution/corrosion products were not considered in calculations.*

(2019) standard was used to estimate TSA porosity.[7] The analysis revealed that the porosity was between 8% and 10% percent for both the TSA and TSA/S coupons. Overall, TSA-coated coupons presented an as-received average coating thickness of 188±55 μm, while TSA/S coupons presented an average thickness of 193±66 μm. Details of the measurements are shown in Table 2.

3.2 | Visual Examination

Figures 6 through 10 show photographs of the coupons retrieved at different times for the bare 25Cr tube with CP, TSA, and TSA/S, with and without CP. The bare 25Cr specimens exhibited more homogeneous and compact deposits than those found on TSA and TSA/S coupons (Figure 6). For all of the specimens, the deposits' areal coverage and thickness on the exposed surfaces increased with exposure time. The minimum deposit growth was observed at 35°C, and the maximum was found at 80°C. Examining the photos of TSA/S coupons also indicates that fewer deposits were seen under CP conditions (Figure 8) than OCP (Figure 7) for low temperatures (20°C and 35°C), whereas at high temperatures (60°C and 80°C), more deposits were observed with CP than those at OCP. The bulk pH inside the tanks was measured at the four temperatures during the first 100 d without substantial changes (7.72 to 7.96 at 20°C, 7.83 to 8.01 at 35°C, 8.01 to 8.11 at 60°C, and 8.29 to 8.15 at 80°C).

3.3 | Characterizing the Deposits

In most cases, the deposits were multilayer, as can be seen in the EDS maps shown in Figure 11. Combining EDS with XRD analyses concluded that the first layer, in contact with metal, was commonly magnesium hydroxide ($Mg(OH)_2$, brucite). The following layer was a mix of magnesium- and calcium-rich deposits, i.e., dolomite ($CaMg(CO_3)_2$) and aragonite ($CaCO_3$), respectively. A summary of the findings is given in Figure 12. As can be seen in Figure 11, the outer biofilm layer on top of the deposits did not present iron traces, suggesting that no rust is observed in Figure 2.

3.4 | Deposit Thickness

The deposit thickness values obtained from the weight gain measurements are shown in Figure 13. The weight gain

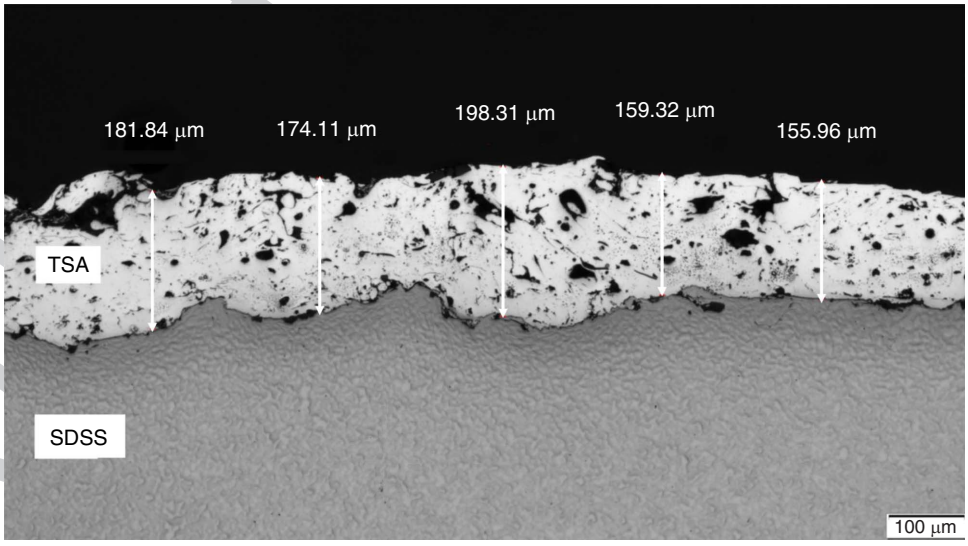

FIGURE 5. *Optical micrograph of a coupon showing coating thickness measurements.*

Table 2. *As-Received Coating Thickness Measurements*

	Thickness (µm)					
	Left		Middle		Right	
Condition/ Specimen	Mean	Std. Dev.	Mean	Std. Dev.	Mean	Std. Dev.
SDSS + TSA	188	49	190	53	187	65
SDSS + TSA/S	173	61	194	82	212	47

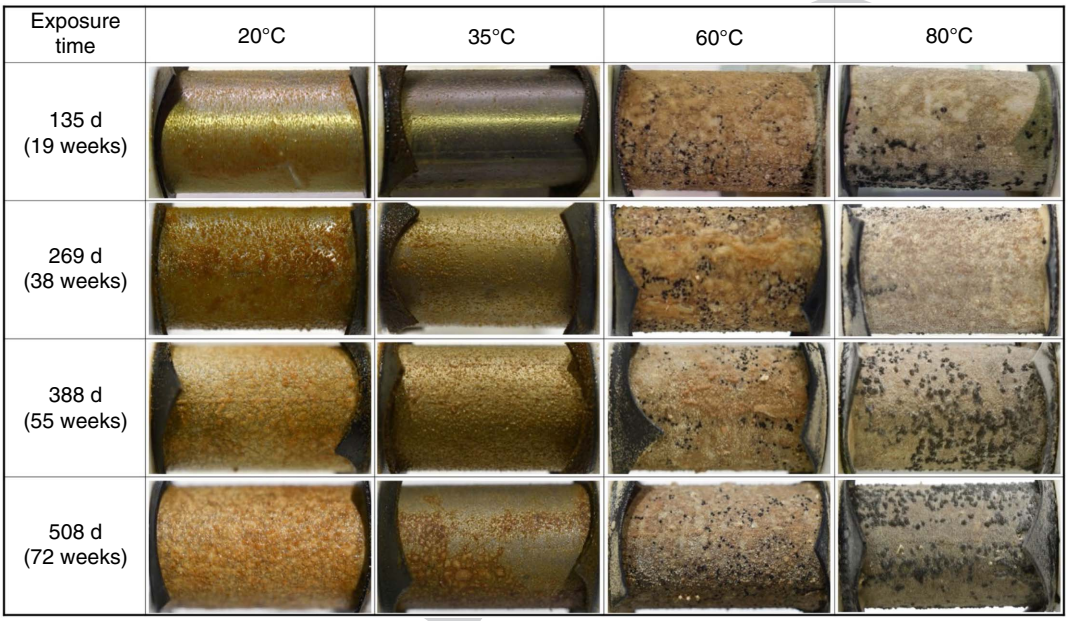

FIGURE 6. *Bare 25Cr coupons with CP, exposed to different temperatures. A thin layer of biofilm formed on the surface of the specimen, which was not visible at higher temperatures.*

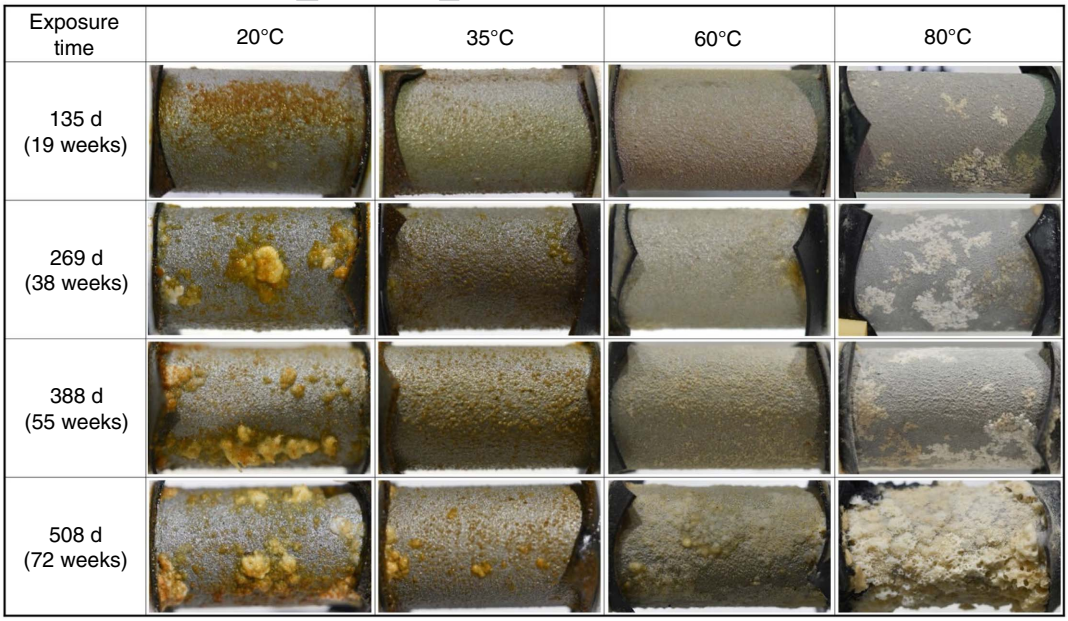

FIGURE 7. *Coupons with TSA/S without CP, exposed to different temperatures. A thin layer of biofilm formed on the surface of the specimen, which was not visible at higher temperatures.*

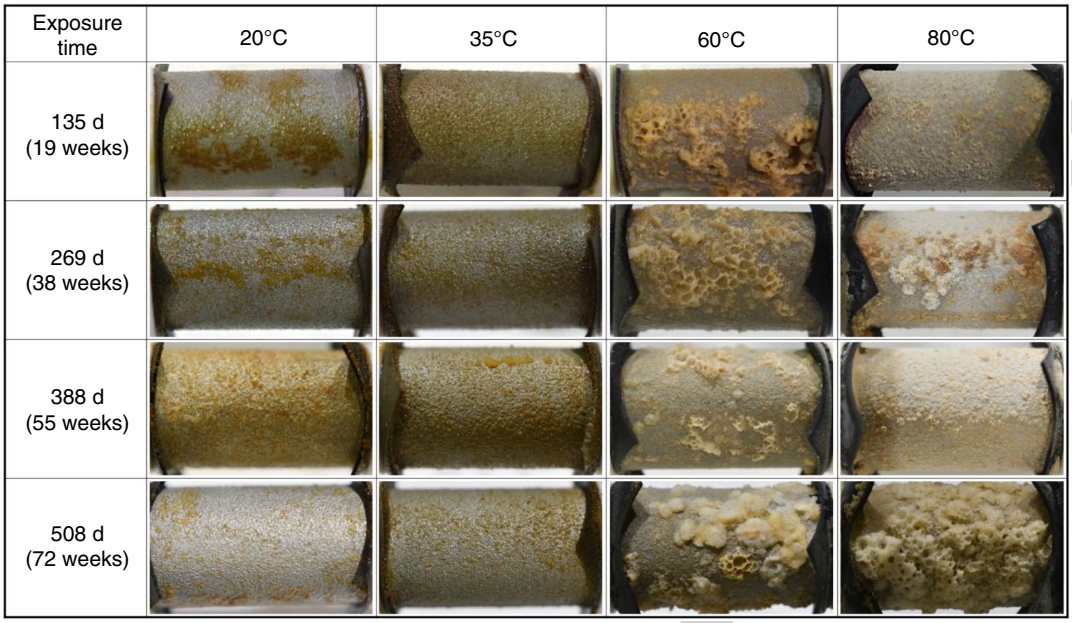

FIGURE 8. *Coupons with TSA/S with CP, exposed to different temperatures. A thin layer of biofilm formed on the surface of the specimen, which was not visible at higher temperatures.*

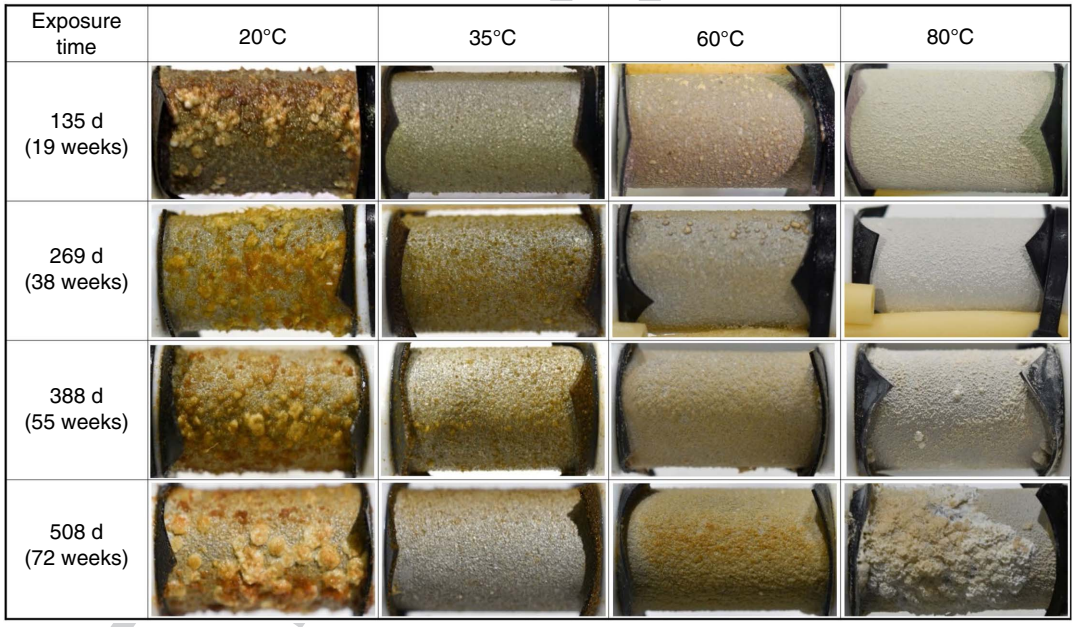

FIGURE 9. *Coupons with TSA without CP, exposed to different temperatures. A thin layer of biofilm formed on the surface of the specimen, which was not visible at higher temperatures.*

increased with increasing temperature, with a drastic growth for the coupons with CP compared to those at OCP.

3.5 | Potential and Cathodic Current Density

Figures 14 through 16 summarize the OCP and the cathodic current densities recorded before each extraction. The mean value and the standard deviation of the coupons submerged up to each retrieval were represented. The TSA (Figure 14) and TSA/S (Figure 15) specimens showed an increase (less negative) in OCP with time for all temperatures. The potentials recorded before the fourth extraction increased with temperature, with an absolute difference of approximately 0.20 V from 20°C to 80°C. A similar difference with the OCP was seen for the TSA/S specimens. Before the first retrieval, both coated coupons (TSA and TSA/S) presented OCP values lower than −1.05 V_{SSC}, except for the coupons at 20°C, in which OCP was slightly above −1.05 V_{SSC}.

Other studies have seen a quicker OCP stabilization on SDSS with TSA-coated coupons in artificial seawater at room temperature.[8] Those studies recorded an OCP of −0.80 V_{SSC} after 30 d of exposure, while it took 250 d to reach a similar value herein. The corrosivity of seawater is not only related to its

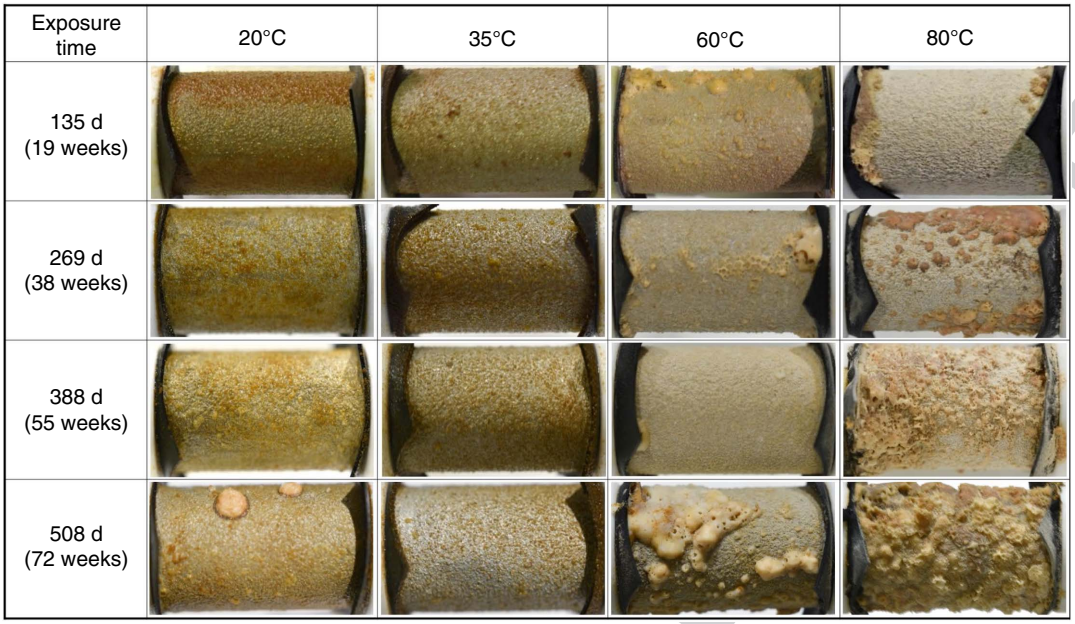

FIGURE 10. *Coupons with TSA with CP, exposed to different temperatures. A thin layer of biofilm formed on the surface of the specimen, which was not visible at higher temperatures.*

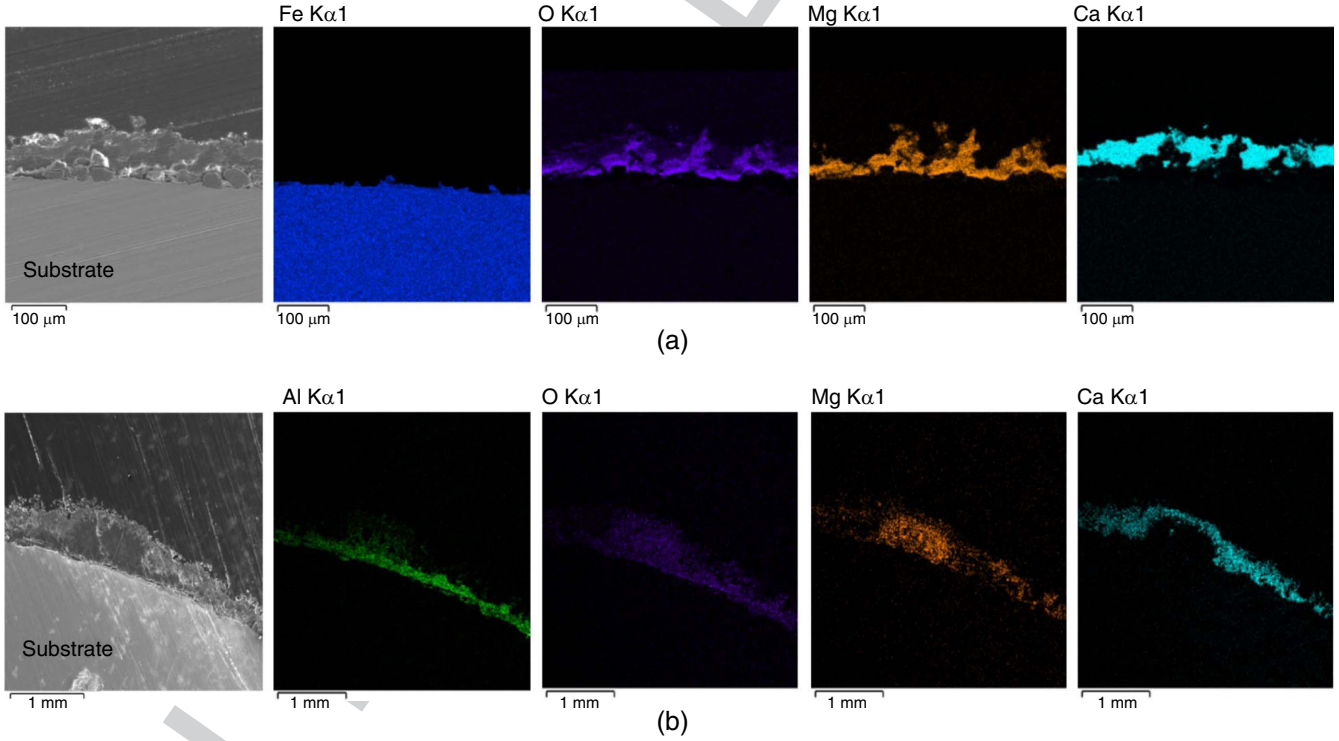

FIGURE 11. *EDS maps on (a) bare 25Cr coupon under CP at 35°C, and (b) TSA coated coupon under CP at 80°C, following the 4th retrieval.*

chemical and physical properties but also its biological activity. This is the reason why synthetic seawaters—which are based only on chemical composition—often lead to different behavior than tests performed in natural seawater.[9] Fischer, et al.,[10] observed OCP values near −0.97 V_{SSC} and −0.98 V_{SSC} after 65 d of exposure to natural seawater, and similar values were obtained to that of this study. The authors also noticed no measurable difference in the OCP values of TSA. For the SDSS (25Cr7Ni3.6Mo) with TSA/S (Al-silicone) at 90°C, Paul, et al.,[8] measured −1.15 V_{SSC} after 90 d, which was a similar value to that obtained herein at the same conditions and exposure duration at 80°C (Figure 15). Ce and Paul[11] measured an OCP of −0.80 V_{SSC} on TSA coupons after 5,000 h (≈210 d) of exposure, similar to that measured in the present work (Figure 14).

OCP measurement on the B specimens began between the first and second retrievals (day N° 193). The OCP on

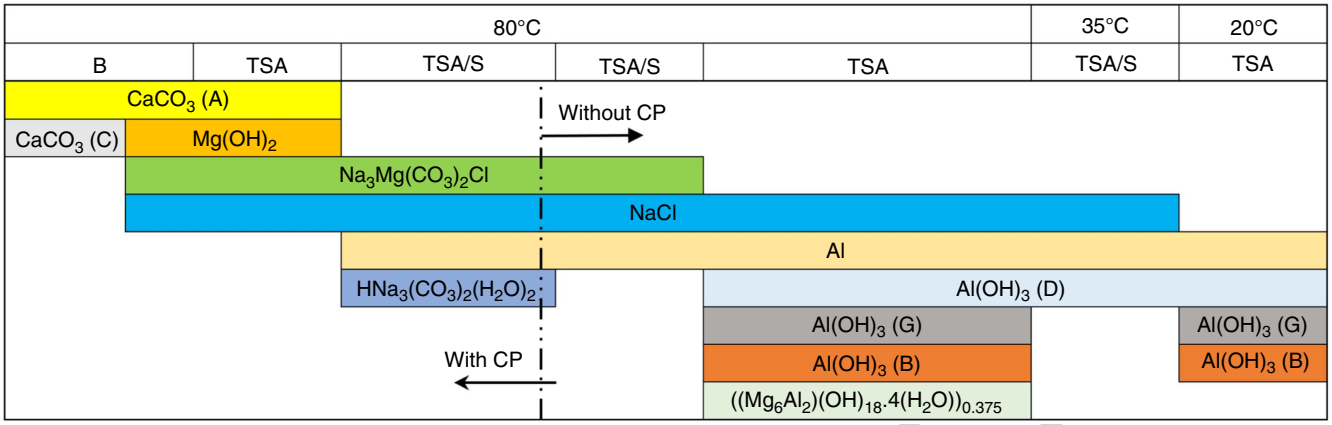

FIGURE 12. *XRD deposit analysis (A: Aragonite, C: Calcite, D: Doyleite, G: Gibbsite, and B: Bayerite).*

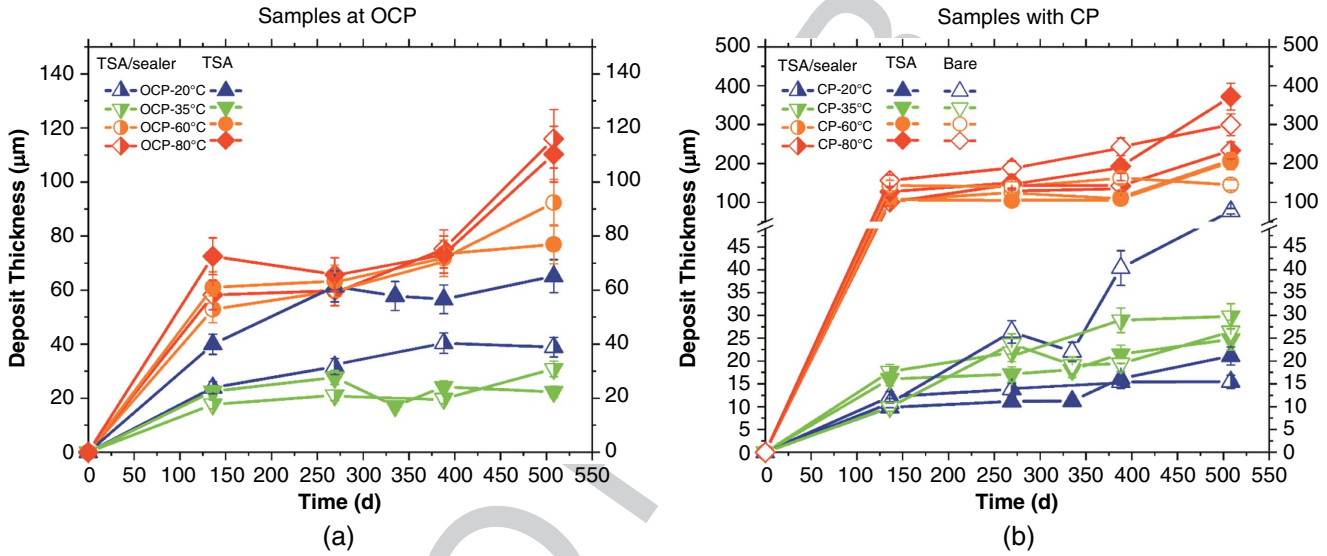

FIGURE 13. *Deposit thickness obtained from the weight-gain measurements on coupons (a) without CP and (b) with CP.*

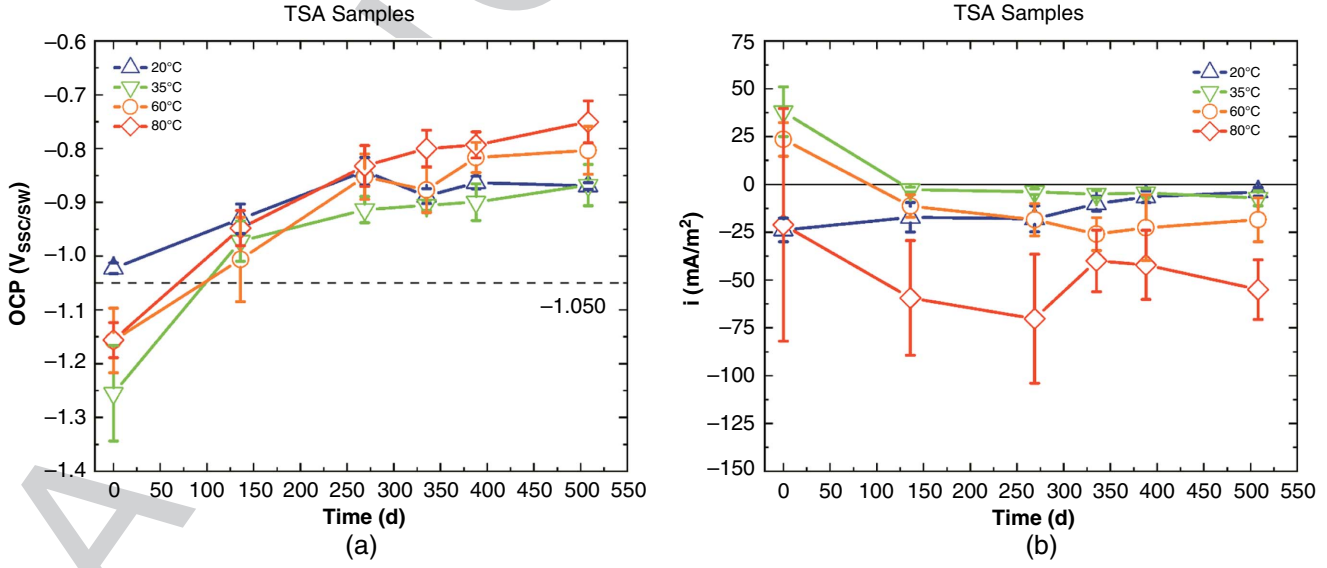

FIGURE 14. *(a) OCP for TSA coupons with time and temperature, and (b) net cathodic current from CP for TSA coupons with time and temperature, before each retrieval.*

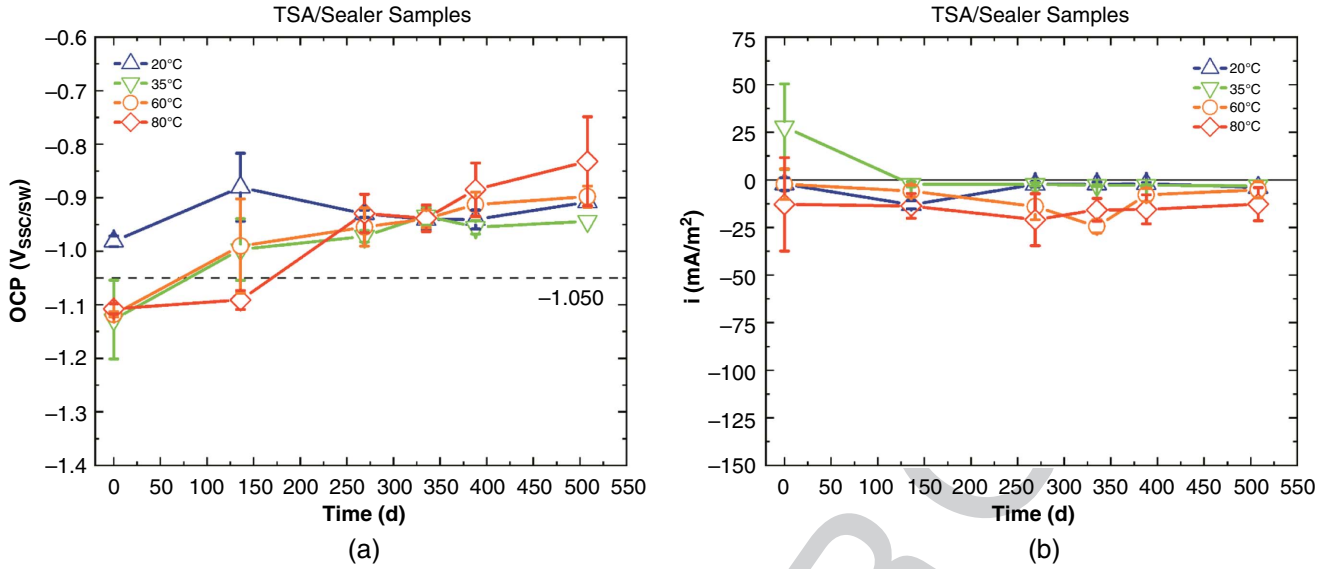

FIGURE 15. *(a) OCP for TSA/S coupons with time and temperature, and (b) net cathodic current for TSA/S coupons with time and temperature, before each retrieval.*

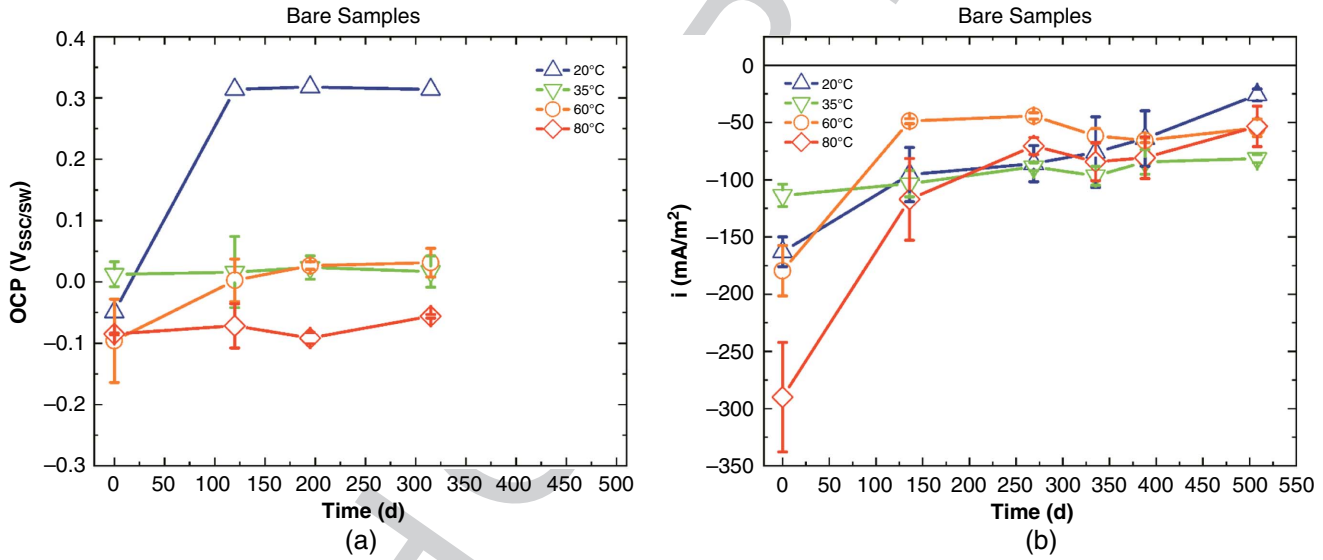

FIGURE 16. *(a) OCP for bare 25Cr coupons with time and temperature, and (b) net cathodic current for bare 25Cr coupons with time and temperature, before each retrieval.*

the B specimens (Figure 16) was higher than those recorded with the TSA coating. In contrast to coated coupons, the OCP over B coupons decreased with temperature. The corrosion potentials at 20°C stabilized at relatively high values, close to +0.30 V_{SSC}. A similar potential (≈ +0.37 V_{SSC}) and the observed fast stabilization followed by a much lower rate during the remaining period were observed in other stainless steels at similar conditions.[12] The incubation time, defined as the delay before a sharp OCP increase, was approx—100 d in our experiments. Feron[13] observed a high variation in incubation times over stainless steels, ranging from 1 d to 120 d. The OCP of the B coupons at 80°C was between −0.05 V_{SSC} and −0.10 V_{SSC}. Paul, et al., measured −0.20 V_{SSC} at 90°C after 3 months of exposure to artificial seawater.[8-9]

The current density values from the CP application decreased (in absolute value) with the exposure time. A large dispersion in current values was observed for coupons with TSA at 80°C (Figures 14 and 15). Fischer, et al., observed cathodic current density values near 30 mA/m^2 to 50 mA/m^2 on TSA-coated steels at 70°C to 100°C after 1 y polarization at −1.10 V_{SSC}.[10] The results of this study were similar to the present investigation. Van Bokhors, et al., measured similar cathodic current values (–10 mA/m^2 to −50 mA/m^2 from room temperature to 95°C) over TSA coupons at −1.10 V_{SSC}.[14] The current measurements from these authors showed a high instability, mainly for the higher temperatures. Positive currents were generally observed at the beginning for the coated alloys. The currents recorded on the B specimens were approximately twice the currents registered for the coated specimens.

DISCUSSION

Calcareous deposit formation on the surface of cathodically protected metallic structures is a well-known process.[15] Cathodic protection gives rise to an increase in the interfacial pH, leading to different types of deposits.[16-17] In most cases, the deposits are multilayer, where the first layer is magnesium hydroxide ($Mg(OH)_2$, brucite). The following layer is often a mix of magnesium- and calcium-rich deposits, i.e., dolomite ($CaMg(CO_3)_2$) and aragonite ($CaCO_3$), respectively.[15] The formation of these deposits can be beneficial as they decrease the required cathodic current density; hence, in the case of sacrificial cathodic protection, for example, the lifetime of the anodes increases.[6] On the other hand, excessive deposit formation can have detrimental effects, such as increasing structure weight or reducing heat exchangers' efficiency.

In this study, a comprehensive experimental investigation was performed to quantify the rate and extent of calcareous scales, cathodic protection potential, and current density requirements for a complex combination of metallic substrates (e.g., with and without TSA coating, the effects of TSA/S) exposed to seawater for 18 months. Specifically, the focus of this work was to:

- Determine the theoretical projected deposit thickness in the 50-y design life of the components. Emphasis was given to the TSA/S case at 20°C and 35°C, considered the most representative scenario.
- Recommend a protection potential and protection current density based on the experimental results of the TSA/S specimens tested at different temperatures.

It should be noted that any discussion and recommendations are solely based on the laboratory tests and may not account for all subsea conditions (e.g., macrofouling and TSA/S degradation). As the DNV RP-B401 code does not provide guidelines for the specific requirements of the heat exchanger, e.g., temperature effects and steady-state current consumption, especially on TSA-coated surfaces, the objectives of this long-term investigation were to provide CP protection potentials and current densities to aid in the CP design of subsea heat exchangers. The CP protection potential is used to determine the correct sacrificial anode material and the current density to determine the anode mass needed. In this case, industry-standard AlZnIn anodes will provide adequate protection as their OCP is below the protection potential found in our work.

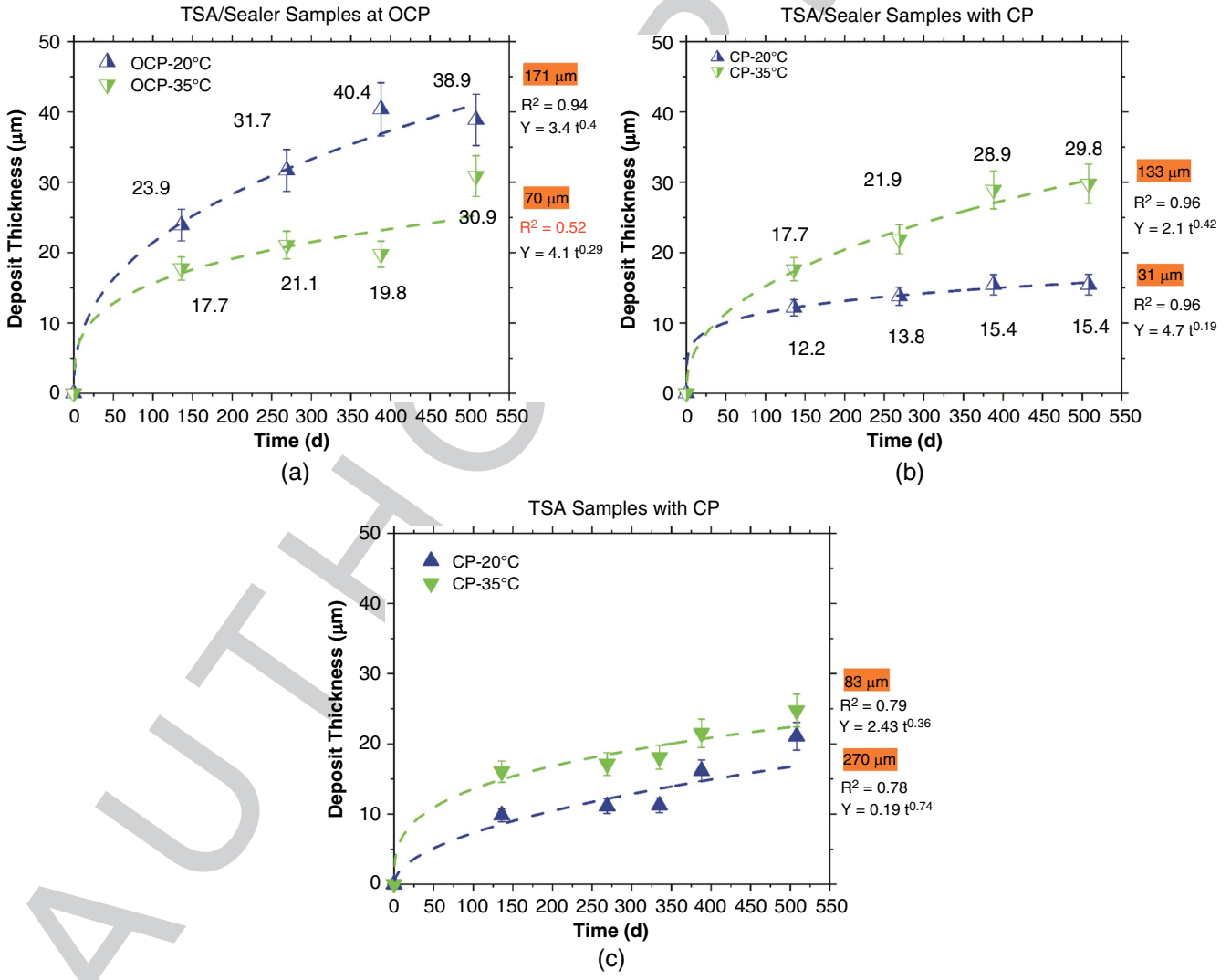

FIGURE 17. *(a) TSA/sealer at OCP, (b) TSA/sealer with CP, and (c) TSA coupons with CP fitted with power function trend line, the orange box provides an estimate of the thickness after 50 y.*

Table 3. *The Final Cathodic Current Density and OCP of the TSA/Sealer Specimen After 508 d of Testing*[A]

	TSA/Sealer		DNV RP-B401		Recommendation	
Temp (°C)	i_{cath} (mA/m^2)	OCP (V_{SSC})	i_{cath} (mA/m^2)[B]	OCP (V_{SSC})[C]	i_{cath} (mA/m^2)	OCP (V_{SSC})
20	−4.3	−0.908	−110.0	−1.050	−8.0	−0.900
35	−3.2	−0.944				
60	−5.2	−0.898			−15.0	
80	−12.8	−0.832				

[A] The recommended cathodic current density and OCP is also given in the table.
[B] The value recommended in Table 10.1 of DNV RP-B401 2010 is for bare alloys in the depth of 100 m to 300 m and subtropical conditions.
[C] The potential is for Al-based anodes taken from Table 10-6 of DNV RP-B401 2010.

4.1 | Calcareous Deposit Thickness Trend

Deposit formation kinetics were assessed by power function fitting of the thickness vs. time data at low temperatures, as shown in Figure 17. For the TSA/S with CP specimens, a power function provided a good fitting because the applied potential resulted in a uniform current distribution on the surface. Figure 17 also summarizes the projected thicknesses after a service life of 50 y. The maximum extrapolated thickness of the TSA/S at OCP coupons was 171 µm at 20°C, while under CP, the maximum thickness was 133 µm at 35°C.

The change in deposit thickness with time on the TSA coupons (without a sealer and under CP) at 20°C has shown a poor fitting with the power function, as shown in Figure 17(c). In this regard, the maximum 50 y projected deposit thickness on the TSA coupons under CP was 270 µm and 83 µm, at 20°C and 35°C, respectively, while at a lower temperature, less deposit growth is anticipated to occur.

4.2 | Protection Potential and Current Density

Table 3 provides the final measured OCP and cathodic current density after 508 d of testing for the TSA/sealer condition. According to the aggregated results, a −8 mA/m^2 current density is recommended for temperatures below 60°C, whereas −15 mA/m^2 is recommended above 60°C. The higher cathodic current density proposed for temperatures over 60°C adds a safety margin to the CP design. The recommended minimum protection potential for TSA is −0.90 V_{SSC}. The recommended protection potential is based on evaluating the OCP values measured and assessing polarization curves from the researchers' previous works.[18-20] Figure 15 showed that for high-temperature coupons (60°C and 80°C) the measured OCP was more positive than −0.90 V_{SSC}. For these cases, the recommended protection potential is more cathodic and would ensure no anodic reaction on the surface (i.e., mass loss of the TSA through corrosion). For the low-temperature cases, the OCP measured was more negative than −0.90 V_{SSC}. Previous studies have shown that the pitting potential for TSA (99.5% Al) is approx. −0.60 V_{SSC} at 10°C and that increasing temperature to 30°C had no considerable effect on the pitting potential (EP ≈ −0.50 V_{SSC}).[18-19] Hence, the protection potential of −0.90 V_{SSC} is also suitable for low-temperature cases, as the TSA surface would be passive and would not suffer mass loss through active corrosion. Based on these considerations, the protection potential was recommended to be −0.90 V_{SSC}.

CONCLUSIONS

The following conclusions can be drawn based on the 1.5 y of experiments that were performed in this study:

➢ Protection current densities of −8 mA/m^2 and −15 mA/m^2 are recommended for temperatures below and above 60°C, respectively, and the recommended minimum protection potential is −0.90 V_{SSC}.
➢ No evident steady-state thickness growth was found for coupons exposed at 60°C and 80°C. Nevertheless, the use of a sealer reduced the maximum calcareous deposit thickness measured.
➢ The surface deposits collected from the surface of the coupons with CP indicated the formation of mainly aragonite and brucite, and sometimes calcite scales. EDS maps indicated that brucite was formed in contact with the substrate, whereas aragonite was formed closer to the seawater.

ACKNOWLEDGMENTS

The authors wish to thank Aker Solution and Chevron Energy for sponsorship of this research. Access to Curtin University's Microscopy and Microanalysis Facility at John de Later Centre is acknowledged.

References

1. N. Ce, S. Paul, *Coatings* 6, 4 (2016): p. 58.
2. C. Holager, R. Johnsen, K. Nisancioglu, "Corrosion of Thermally Sprayed Aluminum in Flowing Seawater," *CORROSION 2015* (Houston, TX: NACE, 2015).
3. H. Wilson, R. Johnsen, C.T. Rodriguez, S.M. Hesjevik, *Mater. Corros.* 70, 2 (2019): p. 293-306.
4. A. Neville, A.P. Morizot, *J. Cryst. Growth* 243, 3-4 (2002): p. 490-502.
5. W.H. Hartt, *Corrosion* 68, 12 (2012): p. 1063-1075.
6. M. Zamanzade, S. Taghi, Y. Ali, *Anti-Corros. Methods Mater.* 54, 02 (2007): p. 74-81.
7. ASTM Standards (Designation E 2109-01), "Standard Test Methods for Determining Area Percentage Porosity in Thermal Sprayed Coatings" (West Conshohocken, PA: ASTM International, 2019), p. 1-8 (reapproved 2014).
8. S. Paul, Q. Lu, M.D.F. Harvey, *J. Thermal Spray Technol.* 24, 4 (2015): p. 629-636.
9. D. Féron, B. Espelid, V. Scotto, "Comparison of Seawater Corrosivity in Europe: Temperature, Biofilm and Ageing Influences," in Proceedings of Euromat'98. Lisbonne, Portugal, 1998.
10. K.P. Fischer, W.H. Thomason, T. Rosbrook, J. Murali, *Mater. Perform.* 34, 4 (1995): p. 27-35.
11. N. Ce, S. Paul, *Coatings* 7, 4 (2017): p. 52.
12. F. Mansfeld, G. Liu, H. Xiao, C.H. Tsai, B.J. Little, *Corros. Sci.* 36, 12 (1994): p. 2063-2095.
13. D. Feron, "Corrosion Behaviour of Stainless Steel in Thermally Altered Seawater," in European Workshop on Sea Water Corrosion of Stainless Steels—Mechanisms and Experiences, Institute of Materials, London, United Kingdom, 1996, p. 75-84.
14. NACE-2014-4196, "Corrosion of Cathodically Polarized TSA in Subsea Mud at High Temperature," *CORROSION 2014* (Houston, TX: NACE, 2014).

15. C. Carré, A. Zanibellato, M. Jeannin, R. Sabot, P. Gunkel-Grillon, A. Serres, *Environ. Chem. Lett.* 18, 4 (2020): p. 1193-1208.
16. C. Barchiche, C. Deslouis, D. Festy, O. Gil, P. Refait, S. Touzain, B. Tribollet, *Electrochim. Acta* 48, 12 (2003): p. 1645-1654.
17. S.L. Wolfson, W.H. Hartt, *Corrosion* 37 (1981): p. 70-76
18. NACE-2017-8941, "Cathodic Protection by Distributed Sacrificial Anodes—A New Cost-Effective Solution to Prevent Corrosion of Subsea Structures," CORROSION 2017 (Houston, TX: NACE, 2017).
19. NACE-2018-11106, "Cathodic Protection by Distributed Sacrificial Anodes—Performance at Elevated Temperature and in Mud," CORROSION 2018 (Houston, TX: NACE, 2018).
20. NACE-2016-7486, "The Effect of Thermally Sprayed Aluminum (TSA) Coating Damage on the Mechanism of Calcareous Deposit Formation on Steel in Boiling Seawater," CORROSION 2016 (Houston, TX: NACE, 2016).

Queries

AQ1: Please provide postal codes for remaining affiliations **, ***.